Journal of The Electrochemical Society, 2021 **168** 024522

Evidence that Surface-Segregated Sr Phases Can Be Removed in LSCF via Ceria Pre-Infiltration, Are Less Apt to Form in SSC

Yubo Zhang* and **Jason D. Nicholas***,z

Chemical Engineering and Materials Science Department, Michigan State University, 428 South Shaw Lane, 2100 Engineering Building, East Lansing, Michigan 48824, United States of America

Here $Ce_{0.9}Gd_{0.1}O_{1.95-x}$ (GDC) pre-infiltration was performed on 12 vol.% $La_{0.6}Sr_{0.4}Co_{0.8}Fe_{0.2}O_{3-x}$ (LSCF) or $Sm_{0.5}Sr_{0.5}CoO_{3-x}$ (SSC) infiltrated GDC Solid Oxide Fuel Cell cathodes. The addition of 7.5 vol.% of ~40 nm diameter GDC nanoparticles into a ~30 μm thick porous scaffold of partially-sintered, sub-micron GDC particles before LSCF infiltration 1) lowered the temperature needed to produce a LSCF-GDC polarization resistance (R_P) of 0.1 Ohm*cm^2 by ~50 °C, and 2) reduced the amount of 500 h, 650 °C open-circuit LSCF-GDC R_P degradation from ~37% to ~6%. In contrast, GDC pre-infiltration had no effect on the initial SSC-GDC R_P or the 19% in R_P degradation observed during 500 h of 650 °C open-circuit aging. X-Ray Photoelectron Spectroscopy showed that GDC pre-infiltration lowered the concentration of strontium species on the surface of the initial and 650 °C-aged LSCF-GDC, but had no effect on the initial or aged SSC-GDC Sr concentrations. Similarly, Electrochemical Impedance Spectroscopy showed that for both the initial and aged LSCF-GDC, GDC pre-infiltration improved oxygen exchange at the infiltrate-backbone and infiltrate-gas interfaces, but had no effect on the SSC-GDC. Hence, GDC pre-infiltration was concluded to improve LSCF-GDC performance and durability by scavenging exsolved Sr-rich secondary phases that form on the interfaces of LSCF, but not SSC.

© 2021 The Author(s). Published on behalf of The Electrochemical Society by IOP Publishing Limited. This is an open access article distributed under the terms of the Creative Commons Attribution 4.0 License (CC BY, http://creativecommons.org/licenses/by/4.0/), which permits unrestricted reuse of the work in any medium, provided the original work is properly cited. [DOI: 10.1149/1945-7111/abe34e]

Manuscript submitted January 11, 2021; revised manuscript received February 3, 2021. Published February 23, 2021.

Supplementary material for this article is available online

Mixed Ionic Electronic Conducting (MIEC) particles that conduct both oxygen ions and electronic species (i.e. electrons or holes) are used as oxygen exchange catalysts in a variety of applications including Solid Oxide Fuel Cells (SOFCs),[1] Solid Oxide Electrolysis Cells (SOEC),[2] catalytic reactors,[3] gas sensors,[4] and oxygen purification membranes.[5] Although a variety of Mixed Ionic Electronic Conductors (MIECs) exist, ABO_3 perovskite-structured transition metal oxides (i.e. cobaltite, ferrites, titanates, etc.) have received considerable attention for the aforementioned applications because their low oxygen surface exchange resistance (R_S) values are associated with fast oxygen reduction reaction (ORR) and oxygen evolution reaction (OER) kinetics.[6,7] Of these, lanthanum strontium cobalt iron oxide (LSCF) is one of the most widely used and researched MIECs for intermediate temperature (IT), i.e. 500 °C–700 °C, SOFC cathode operation.[6,8] Unfortunately, even though LSCF has a low R_S, its bulk oxygen ion conductivity ($\sigma_{V_O^{\cdot\cdot}}$) is lower than competing materials.[6,9,10] Hence, its performance can be improved (compared to porous, single-phase, sintered micro-particulate LSCF cathodes) by producing large quantities of nano-sized LSCF particles (that maximize the surface area available for oxygen exchange) atop porous, sintered micro-particulate gadolinium doped ceria (GDC) backbones (that promote efficient bulk oxygen ion conduction to the electrolyte).[11,12] These Nano-Composite Cathodes (NCCs) typically have microstructures similar to those shown in Fig. 1.[13]

In addition, past studies have found that the oxygen exchange kinetics at the LSCF-gas interface can be improved through the addition of doped ceria particles.[15–17] This curious behavior also occurs in other MIECs such as lanthanum strontium cobaltite,[16] lanthanum strontium ferrite,[16] strontium iron molybdenite,[18] lanthanum strontium titanate,[19] lanthanum strontium manganate,[20] and lanthanum iron nickelate.[21] This is surprising because the bulk GDC oxygen surface exchange coefficient is several orders of magnitude lower than that of LSCF in air at a typical IT-SOFC operating temperature of 650 °C,[22,23] suggesting that (for all practical purposes) oxygen should only exchange into/out of LSCF, and not GDC, when LSCF and GDC are parallel oxygen exchange pathways. To explain this apparent conundrum, mechanisms such as impurity cleanup of the doped ceria surface by LSCF that could make the GDC surface active for oxygen exchange,[24,25] spillover of the LSCF oxygen exchange reaction onto the doped ceria surface,[17,25,26] transition metal doping of the doped ceria surface by LSCF that could make the GDC surface active for oxygen exchange,[24] and doped ceria-LSCF heterojunction-induced changes in lattice strain/charge/point defect concentrations that could enhance oxygen surface exchange on the LSCF and/or GDC surfaces[27–29] have all been proposed. However, consensus on which mechanism(s) are active has remained elusive. Further, although some studies exist,[30,31] the impact of ceria on the oxygen exchange properties of other SOFC materials, such as $Sm_{0.5}Sr_{0.5}CoO_{3-x}$ (SSC), is less documented than the impact of ceria on LSCF.

Hence, the objective of the present work was to document and understand the impact of GDC nano-particle additions on the performance and 650 °C aging behavior of LSCF-GDC and SSC-GDC NCCs.

This was achieved by infiltrating gadolinium and cerium nitrate solutions into traditional GDC NCC backbones before subsequent LSCF or SSC infiltration. Compared to alternative techniques such as the deposition of doped ceria thin films on LSCF,[29] the mixing and sintering of bulk LSCF and bulk doped ceria powders,[24–26] and the surface decoration of LSCF with doped ceria nanoparticles,[17] this novel GDC pre-infiltration approach allowed various possible GDC-enhancement mechanisms to be excluded by allowing the GDC volume percentage and surface area to be dramatically increased without changing or covering the LSCF or SSC surface area.

Experimental

Cell fabrication.—Symmetric, electrolyte-supported NCC-electrolyte-NCC cells were fabricated for the experiments here in the following manner. First, GDC discs were fabricated by pressing ~1.2 g of $Ce_{0.9}Gd_{0.1}O_{1.95-x}$ powder (Rhodia, Cranbury, NJ) with a uniaxial press (Model 3851, Carver Inc., Wabash, IN) to ~40 MPa using a ~20 mm central diameter stainless steel die. The pressed GDC discs were then sintered at 1450 °C for 20 h using nominal heating and cooling rates of ~3 °C min^{-1} to achieve a sintered GDC relative density > 93%. After sintering, the GDC pellets were sanded down to ~0.5 mm in thickness using 120 grit SiC sandpaper

*Electrochemical Society Member.
zE-mail: jdn@msu.edu

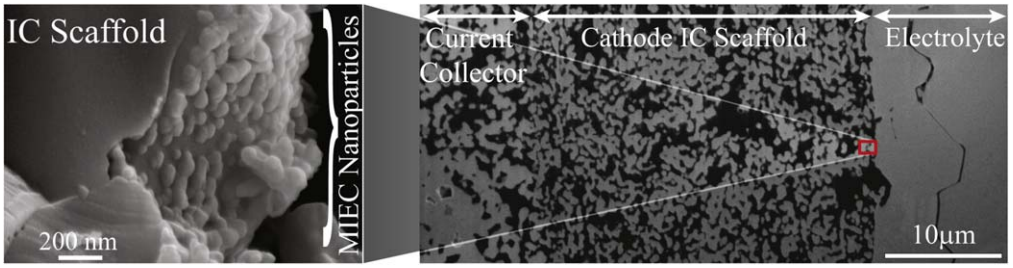

Figure 1. Representative Scanning Electron Micrographs of a nano-composite Solid Oxide Fuel Cell cathode made of Mixed Ionic Electronic Conducting (MIEC) nano-particles ($La_{0.6}Sr_{0.4}Co_{0.8}Fe_{0.2}O_{3-x}$) atop a sintered Ionic Conducting (IC) scaffold ($Ce_{0.9}Gd_{0.1}O_{1.95-x}$). Reproduced with permission from Burye and Nicholas.[14]

to serve as mechanically-supporting symmetric cell electrolyte layers.

Second, porous GDC scaffold layers were screen printed onto both sides of the sanded GDC pellets. The GDC paste used for screen printing was prepared by three-roll-milling $Ce_{0.9}Gd_{0.1}O_{1.95-x}$ powder (Rhodia, Cranbury, NJ) coarsened at 800 °C for 4 h with electronic vehicle (V-737, Heraeus, West Conshohocken, PA) in a 1:2 mass ratio. The homogenized GDC ink was then screen printed onto both sides of each GDC pellet using a 12 inch × 12 inch, 80-mesh stainless steel screen with a circular pass-through area of 0.5 cm^2. The screen wire diameter was 0.051 mm and the mesh pattern had a 70.5% open area percentage. After the deposition of each new screen-printed layer, the ink was allowed to flow in air for 5 min (to promote layer thickness homogenization) and then the solvent was removed via drying in a 120 °C oven for 5 min. This procedure was repeated, as necessary, to reach a desired sintered GDC scaffold thickness of ~30 μm. The cells were then heated at 3 °C min^{-1} to 400 °C, held at 400 °C for 1 h to promote organic burn-out, heated at 3 °C min^{-1} to 600 °C, held at 600 °C for 1 h to complete organic burnout, heated at 3 °C min^{-1} to 1100 °C, held at 1100 °C for 3 h to promote GDC particle necking within the screen-printed layers, and cooled to room temperature with a nominal 5 °C min^{-1} cooling rate. The resulting thickness of the GDC scaffold layers were then measured with a profilometer (Dektak, Bruker, Billerica, MA).

Third, GDC nitrate precursor solutions were infiltrated into, and then thermally decomposed within, the pores of the GDC scaffolds. These precursor solutions were produced by first dissolving 3 wt% of Triton-X 100 (Alfa Aesar, Haverhill,) into 18.2 MOhm-cm MilliQ water via room temperature stirring for 10 min. Then, stoichiometric amounts of high-purity (> 99.9% pure on a metals basis) $Gd(NO_3)_3$*6 H_2O and $Ce(NO_3)_4$*6 H_2O, (Alfa Aesar, Haverhill, MA) were added to form GDC with a 1:9 Gd:Ce atomic ratio. The resulting 1.5 molar (total moles of cations per liter) precursor nitrate solution was then stirred for 10 min before being pipetted into the porous GDC scaffolds on both sides of each GDC electrolyte-supported cell. After each infiltration, each cell was held in air for 5 min, and dried in an 80 °C oven for 10 min in a drying oven. To form infiltrate nano-particles via thermal decomposition of the precursor nitrate solution, the infiltrated cells were then heated in air at 10 °C min^{-1} to 700 °C, held at 700 °C for 1 h, and cooled to room temperature using a nominal 10 °C min^{-1} cooling rate. This infiltration and firing procedure was then repeated a second time to reach the desired GDC nano-particle infiltrate loading level of 7.5 vol.% (volume of the GDC infiltrate/total geometric volume (i.e. the geometric area times the cathode thickness)).

Fourth, LSCF or SSC nitrate precursor solutions were infiltrated into, and then thermally decomposed within, the pores of the GDC scaffolds. The 1.5 molar (total moles of cations per liter) LSCF precursor solutions were made in the same manner as the GDC precursor solutions except that $La(NO_3)_3$*6 H_2O, $Sr(NO_3)_2$, $Co(NO_3)_2$*6 H_2O, and $Fe(NO_3)_3$*9 H_2O (Alfa Aesar, Haverhill, MA) were added in a 6:4:8:2 La:Sr:Co:Fe atomic ratio. The 1.5 molar (total moles of cations per liter) SSC precursor solutions were made in the same manner as the GDC precursor solutions except that $Sm(NO_3)_3$, $Sr(NO_3)_2$, and $Co(NO_3)_2$*6 H_2O (Alfa Aesar, Haverhill, MA) were added in a 1:1:2 Sm:Sr:Co atomic ratio. Three rounds of infiltration + firing were used to achieve the desired 12 vol% of LSCF or SSC. Except for the fact that the SSC had to be fired to 800 °C instead of 700 °C to produce the requisite infiltrate phase purity, identical processing procedures were used to produce the LSCF-GDC and SSC-GDC NCCs examined here. (Note, studies on NCCs with the best possible peformance (i.e. those with the highest possible infiltrate surface area that still contained the requisite infiltrate phase purity) were deemed more intersting than NCCs where the LSCF and SSC were fired to the same temperature).

Lastly, current collecting layers were screen printed atop each infiltrated cathode. For this purpose, $(La_{0.8}Sr_{0.2})_{0.98}MnO_{3-x}$ (LSM) paste was prepared by mixing LSM powder (Praxair Surface Technologies, Woodinville, WA) with V-737 electronic vehicle (Heraeus, West Conshohocken, PA) in a 1:2 mass ratio. After homogenizing the paste in a three-roll-mill, the LSM was screen printed onto each NCC using a 12 inch × 12 inch, 325-mesh stainless steel screen with a circular pass-through area of 0.5 cm^2. The screen wire diameter was 0.023 mm and the mesh had a 60% open area percentage. After each printing, the ink was held in air for 5 min (to promote LSM thickness uniformity through ink flow), and then dried in a 120 °C oven for 5 min. The LSM coated cells were then heated to 700 °C for an hour using 10 °C min^{-1} nominal heating and cooling rates. To promote current collection without blocking O_2 transport, gold paste (C5756, Heraeus, West Conshohocken, PA) was then screen printed on both sides of the cells in an orthogonal grid pattern and dried at 80 °C for 10 min before electrochemical characterization.

LSCF-GDC and SSC-GDC NCCs for XPS analyses were fabricated similarly, but without the application of LSM or gold current collecting layers.

In addition, due to peak overlap between the GDC and the LSCF or SSC X-ray Diffraction (XRD) signals, LSCF and SSC powders for XRD analyses were fabricated by firing precursor nitrate solutions on alumina plates (i.e. outside GDC scaffolds). Specifically, LSCF powder was fabricated by firing LSCF precursor nitrate solution at 700 °C for an hour in air using nominal heating and cooling rates of 10 °C min^{-1}. SSC powder was fabricated similarly, but with a firing temperature of 800 °C. An evaporation surface area ratio (i.e. the volume of infiltrate solution/geometric surface area it was spread onto)[32] of ~500 μm was used for both the LSCF and GDC powders during precursor solution firing. To investigate the possible reaction between LSCF or SSC and the GDC nano particles, LSCF or SSC powder was also fabricated with GDC nano-particles, outside a cathode. The LSCF + GDC powders were made by first firing GDC precursor nitrate solution on alumina plates at 700 °C for an hour with a 10 °C min^{-1} heating/cooling rate to form nano-sized GDC powders. Then, ~3 ml of LSCF precursor nitrate solution was infiltrated into ~1 g of GDC powder and fired at 700 °C for an hour with 10 °C min^{-1} heating/cooling rates. The SSC + GDC powder for XRD analyses were fabricated similarly, but with an 800 °C firing temperature.

Characterization.—XRD scans were conducted using a Miniflex II (Rigaku, The Woodlands, TX) to scan 2 θ angles from 20° to 80°

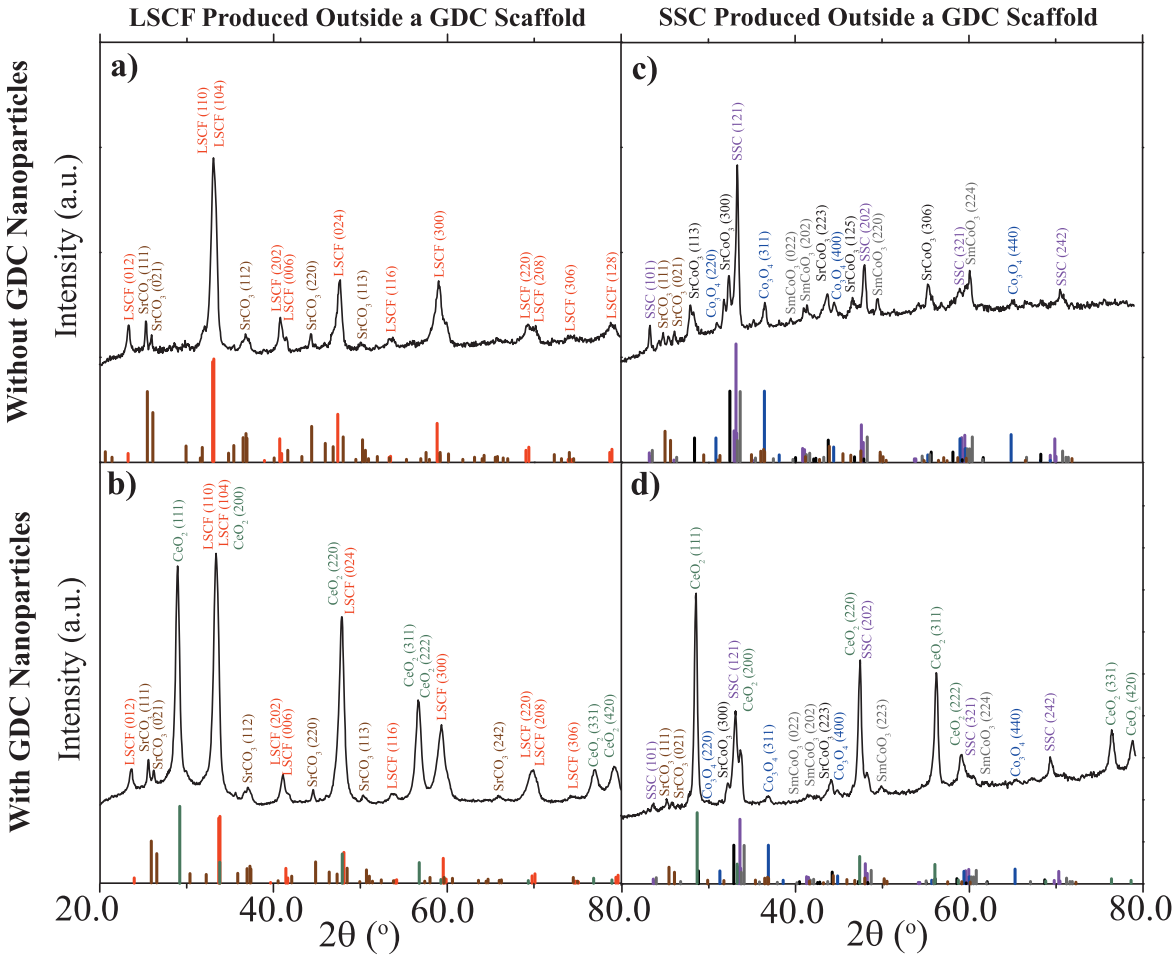

Figure 2. X-ray diffractograms of (a)–(b) LSCF and (c)–(d) SSC powders produced outside of a GDC scaffold (b), (d) with and (a), (c) without nano-sized GDC particles present. The underlying reference XRD patterns are CeO_2 Powder Diffraction File (PDF) # 01–073–7747, Co_3O_4 PDF # 00–043–1003, $La_{0.6}Sr_{0.4}Co_{0.8}Fe_{0.2}O_{3-x}$ PDF # 01–048–0124, $SmCoO_3$ PDF # 00–025–1071, $Sm_{0.5}Sr_{0.5}CoO_{3-x}$ PDF # 00–053–0112, $SrCO_3$ PDF # 00–005–0418, and $SrCoO_3$ PDF #00–049–0692.

with a scan speed of 1° min^{-1} and a sampling width of 0.05°/step. All XRD scans were performed with a copper target, a nickel filter, a 1.25 degree divergence slit, a 0.3 mm receiving slit, a 30 kV voltage, and a 15 mA current.

NCC electrochemical performance was evaluated via Electrochemical Impedance Spectroscopy (EIS). All EIS measurements were conducted from frequencies of 100 kHz–0.1 Hz with a nominal 100 mV AC amplitude using an IM6 impedance analyzer (Zahner, Kronach, Germany). Due to the ∼1.8 meter-long leads used to connect the impedance analyzer to the samples deep within the oven, a nominal 100 mV signal corresponded to ∼75 mV across the sample. Select experiments using nominal AC amplitudes of 50 mV (∼25 mV across the sample) gave identical, but noisier, impedance curves. Impedance data was collected every 50 °C from 400 °C to 700 °C using the spring-loaded Pt plate push-contact and Pt lead wire electrical setup shown in Fig. S1 (available online at stacks.iop.org/JES/168/024522/mmedia) of the Supplemental Materials. At each temperature, each cell was held for at least 20 min before testing to ensure thermal equilibrium. The electrode polarization resistance (R_P) for each NCC was determined from the distance between the two *x*-axis intercepts on an EIS Nyquist plot. The ohmic resistance (R_0) was determined from the distance from the EIS Nyquist plot origin to the high-frequency x-intercept. For controlled-atmosphere EIS tests, $O_2 + N_2$ gas mixtures with 5%, 20% and 40% oxygen were introduced, respectively, with 100 sccm flow rates. All cells were held for at least 15 min after gas atmosphere switching, and before EIS testing, to ensure the homogeneity of the testing atmosphere. Equivalent circuit impedance fitting was performed using the Zview software package (Scribner Associates, Southern Pines, NC).

NCC microstructure was investigated via Scanning Electron Microscopy (SEM, Auriga, Carl Zeiss, White Plains, NY) on 1 nm platinum-coated NCC fracture surfaces. A 20 kV voltage beam and a ∼4 mm working distance were used for SEM analyses. To avoid confusion with small GDC backbone particles, the SEM images used to perform infiltrate particle size measurements were taken within electrolyte cracks at the electrolyte-electrode interface, as done previously.[12,14–16,32,33,34,35]

NCC surface elemental analyses were conducted via X-ray Photoelectron Spectroscopy (XPS, Phi 5600, Perkin Elmer, Waltham, MA). All XPS analyses were performed using an Al X-ray target with an accelerating voltage of 20 kV and a testing area of 1 mm by 3.5 mm. XPS survey scans were conducted with a step size of 0.4 eV and a pass energy of 187.5 eV. In contrast, detailed elemental scans were collected with a step size of 0.1 eV and a pass energy of 23.75 eV. The relative atomic concentration for the different elements and the Sr 3d peak deconvolutions were determined from detailed elemental scans using the Multipak software package. Specifically, Sr 3d peak deconvolution was performed by first calibrating the binding energy of the Sr 3d peaks with the 285.0 eV hydrocarbon C 1 s photoemission peak. Then, following the procedures described in past literature studies,[31,32] the Sr 3d 5/2 and Sr 3d 3/2 doublets with higher binding energies were attributed to "Surface Sr" species like SrO, $Sr(OH)_2$ and/or $SrCO_3$, while Sr

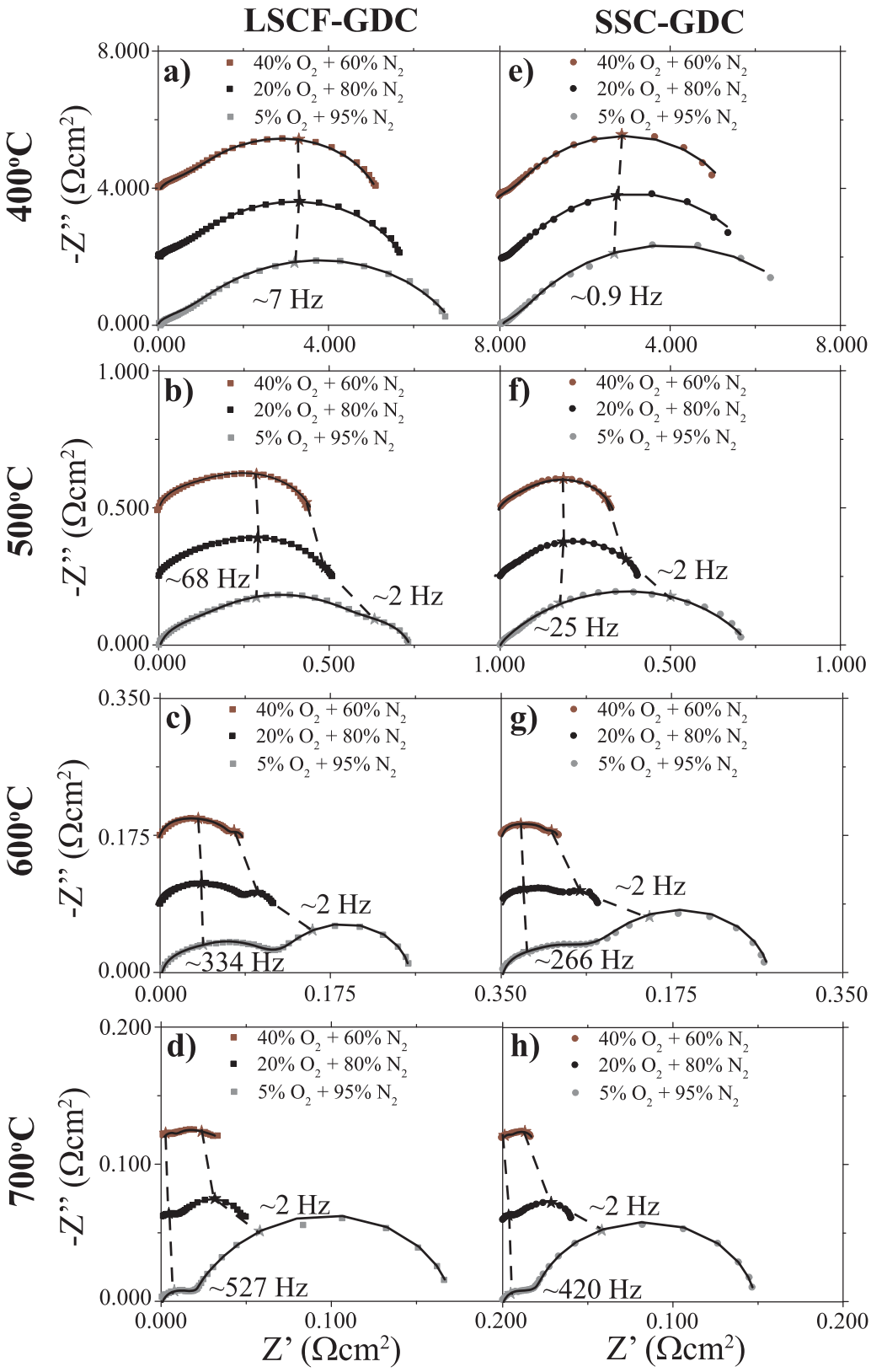

Figure 3. Electrochemical Impedance Spectroscopy Nyquist plots as a function of oxygen partial pressure for bare, 12 vol% (a)–(d) LSCF-GDC, and (e)–(h) SSC-GDC NCCs, before aging, at various temperatures. To ease in comparison, the *x*-axis ohmic offset (which differed by less than 2% between cells) has been removed from the plots. To help the reader identify which frequency regimes are changing with temperature, dashed lines joining points taken at identical frequencies have been added to the plots. High, intermediate and low frequency equivalent circuit resistance values resulting in the fits shown here as black lines are reported in Table S1 of the Supplemental Materials. Additional EIS Nyquist plots taken at 450 °C, 550 °C and 650 °C can be found in Fig. S4 of the Supplemental Materials.

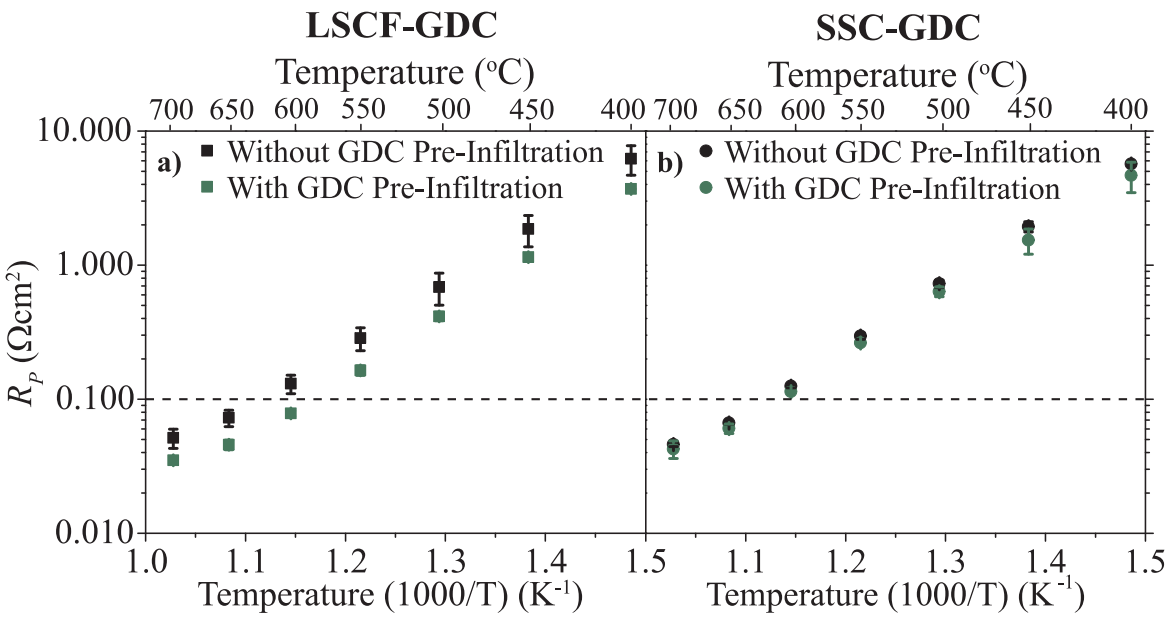

Figure 4. Polarization resistance of 12 vol% a) LSCF-GDC and b) SSC-GDC NCCs, before aging, with and without 7.5 vol% of GDC pre-infiltration. The error bar lengths indicate plus and minus a standard deviation in the polarization resistance of at least three identically prepared NCC symmetric cells.

doublets with lower binding energies were attributed to "Lattice Sr" in a perovskite crystal structure. The relative peak areas of the respective Sr doublets were then calculated and taken as the relative concentrations of the surface and lattice Sr species.

Results

Infiltrate phase purity.—Figure 2 shows that even though firing temperatures of 700 °C and 800 °C were sufficient to produce LSCF and SSC, respectively, as the dominant infiltrate phase, impurity phases remained (likely due to the different solubilities of the different precursor nitrates). Specifically, as shown in Figs. 2a and 2b, with or without nano-GDC present, the LSCF precursor solution thermal decomposition product was mostly perovskite-structured LSCF (with distinct peaks at 33.0°, 47.3° and 58.7°) with some $SrCO_3$ (with distinct peaks at 25.2°, 25.8° and 44.1°). In contrast, as shown in Figs. 2c and 2d, with or without nano-GDC present, the SSC-GDC precursor solution thermal decomposition product was mainly perovskite-structured SSC (with distinct peaks at 33.3° and 70.0°), with some $SrCoO_3$ (with distinct peaks at 32.7° and 55.8°), $SmCoO_3$ (with distinct peaks at 41.8° and 60.0°), Co_3O_4 (with distinct peaks at 36.8° and 65.2°), and $SrCO_3$ (with distinct peaks at 25.2° and 25.8°). These results are consistent with the $SrCO_3$ found in literature LSCF infiltrate produced using Triton X-100 as a chelating agent,[35] and the $SrCO_3$, Co_3O_4, $SmCoO_3$, Sm_2O_3, and/or $SrCoO_3$ found in literature SSC infiltrate produced using Triton X-100 as a chelating agent.[32,34,36] Although quantitative volume percent estimates between phases could not be made due to unknown X-ray adsorption factors for each phase, relative changes in the volume percents between pairs of identical phases observed in multiple plots were possible. These analyses (made after accounting for the peak overlap between the GDC and the MIEC phases) suggested that GDC pre-infiltration did not have a significant impact on the X-ray-detectable LSCF-GDC or SSC-GDC impurity phase concentrations.

Initial electrochemical performance.—Figure 3 shows bare LSCF-GDC and SSC-GDC controlled-atmosphere electrochemical impedance spectroscopy (EIS) results indicating that the high, intermediate, and low-frequency electrochemical response of these cathodes corresponded to oxygen/oxygen ion transport across the infiltrate-backbone interface, into and through the cathode, and through the cathode pores, respectively. Specifically, the 400 °C to ~600 °C bare LSCF-GDC and bare SSC-GDC Nyquist plot are similar in shape to those for literature LSCF-GDC[15,33,14] and SSC-GDC[31,34,36] NCCs which have been successfully modeled with equivalent circuits containing 1) a circuit wiring inductor, 2) a resistor representing the ohmic electronic transport losses in the cathode/current collector/wiring and ionic losses across the electrolyte, and 3) an electrode R_P, all in series. In these previous studies (and duplicated in the equivalent circuit modeling fits shown in Fig. 3 and the results shown in Table S1 of the Supplemental Materials), the electrode R_P was modeled as the in-series summation of a high frequency RQ element attributed to oxygen transport across the solid-solid interface and an intermediate frequency Gerischer element representing oxygen surface exchange and solid state transport within the cathode.[36,37] The major difference in the electrodes reported here is that, as shown in Fig. 3 and Table S1, they contain an additional arc with a low frequency (~2 Hz) characteristic frequency and temperature-independent magnitude that appears at 600 °C in air and becomes the dominant source of resistance by 700 °C in air. Due to this arc's nearly temperature-invariant magnitude and its sensitivity to the diffusivity of O_2 gas (as summarized in Zhang et al.[35] this arc was larger in 20%O_2−80%He mixtures than in 20%O_2−80%N_2 mixtures or air), this arc was concluded to represent O_2 gas concentration polarization within the NCC pores, and was equivalent circuit modelled as a Warburg element as done previously in the literature.[38] Consistent with a gas concentration assignment, this arc grew in size as the Fig. 3 oxygen partial pressure decreased. Consistent with the high frequency response representing transport across the infiltrate-backbone interface and the intermediate frequency response representing cathode oxygen transport, Fig. 3 and Table S1 also show that for both LSCF-GDC and SSC-GDC, the high frequency arc was nearly insensitive to the oxygen partial pressure, while the intermediate frequency arc was not.

Figure 4 shows R_P vs temperature plots indicating that GDC pre-infiltration improved the initial performance of LSCF-GDC cathodes, but not SSC-GDC cathodes. Specifically, the bare 12 vol% LSCF-GDC NCCs produced here achieved a $R_P = 0.1\ \Omega cm^2$ at ~625 °C while the GDC pre-infiltrated 12 vol% LSCF-GDC NCCs achieved a $R_P = 0.1\ \Omega cm^2$ at ~575 °C. The bare and GDC pre-infiltrated LSCF-GDC displayed 400 °C–650 °C R_P activation energies of 0.95 eV and 0.96 eV, respectively, which is similar to the ~1.0 eV 400 °C–650 °C R_P activation energy (E_A) reported

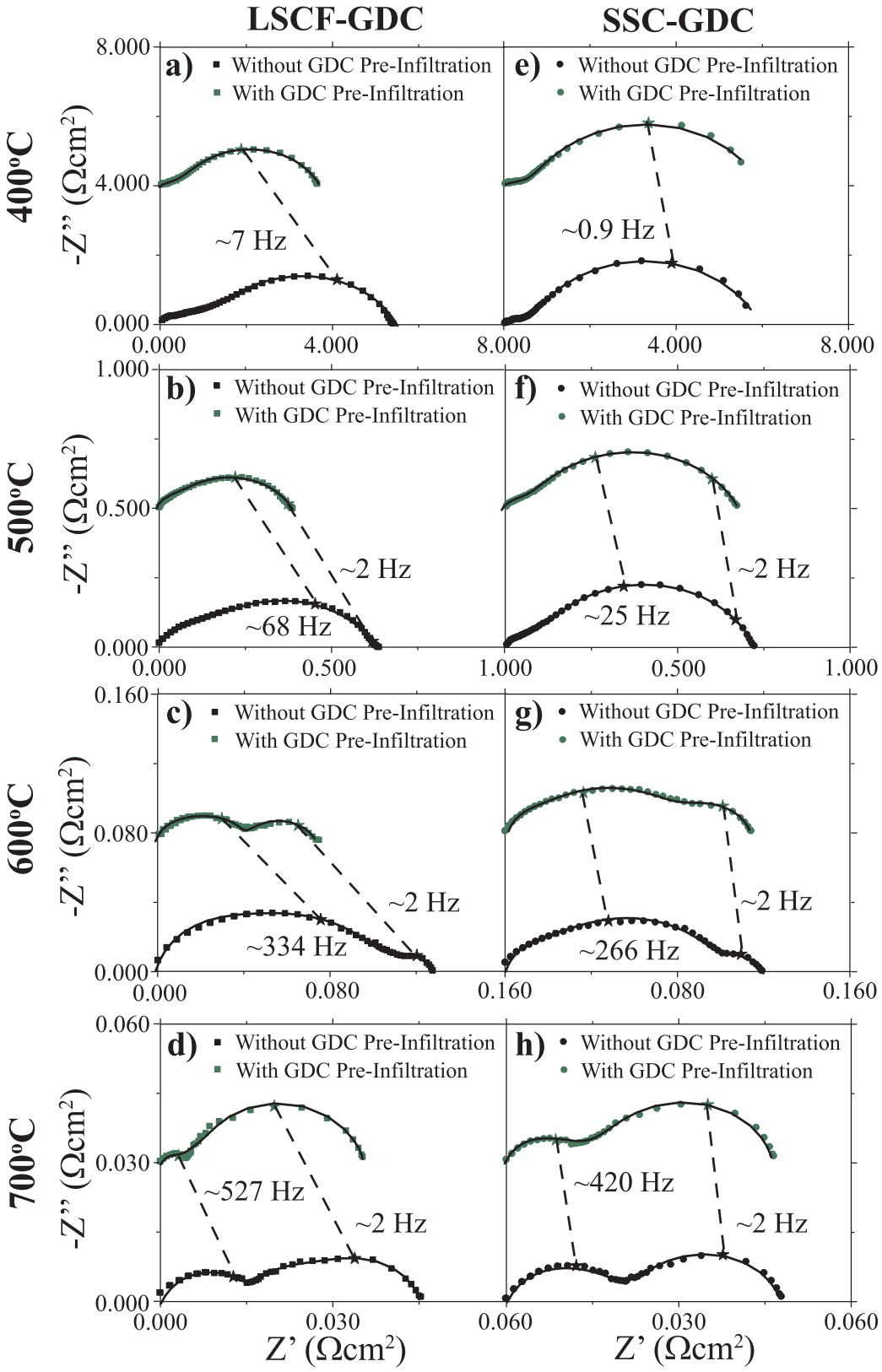

Figure 5. Electrochemical Impedance Spectroscopy Nyquist plots for 12 vol% a–d) LSCF-GDC, and e–h) SSC-GDC NCCs at various temperatures, before aging, with and without 7.5 vol% of GDC pre-infiltration in air. To ease in comparison between cells, the *x*-axis ohmic offset (which differed by less than 2% between cells) has been removed from the plots. To help the reader identify which frequency regimes are changing with GDC pre-infiltration, dashed lines joining points taken at identical frequencies have been added to the plots. High, intermediate and low frequency equivalent circuit resistance values resulting in the fits shown here as black lines are reported in Table S2 of the Supplemental Materials. Additional EIS Nyquist plots taken at 450 °C, 550 °C and 650 °C can be found in Fig. S5 of the Supplemental Materials.

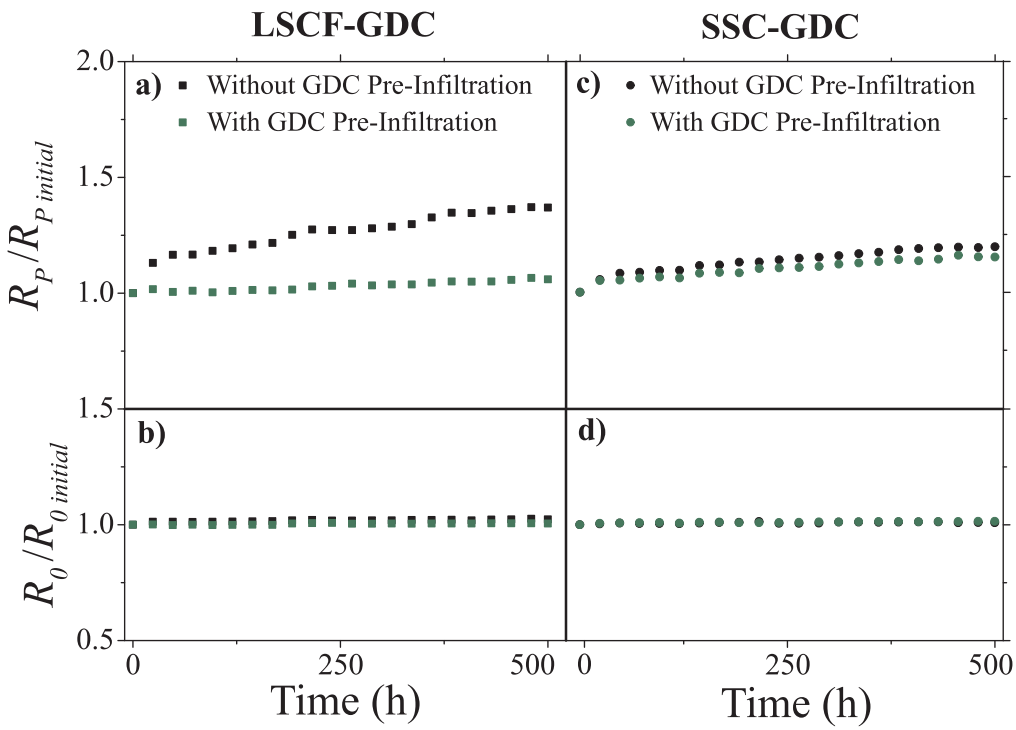

Figure 6. Normalized 12 vol% (a)–(b) LSCF-GDC, and (c)–(d) SSC-GDC 650 °C polarization resistance (top) and ohmic resistance (bottom) degradation behavior, with and without 7.5 vol% of GDC pre-infiltration.

previously for bare and GDC pre-infiltrated LSCF-GDC NCCs.[15] This E_A is consistent with the majority of the Fig. 3 400 °C – 650 °C distance between the *x*-axis intercepts coming from the intermediate frequency oxygen exchange resistance (as shown numerically in Table S1), previous Simple Infiltrated Microstructure Polarization Loss Estimation (SIMPLE) modeling which showed that oxygen surface exchange into the infiltrate dominates over oxygen diffusion in the GDC backbone to determine R_P in 12 vol% LSCF-GDC NCCs below ∼650 °C,[32] and the 1.1 eV 425 °C–525 °C oxygen surface exchange resistance E_A reported for LSCF thin films.[8] The bare and GDC pre-infiltrated LSCF-GDC displayed 650 °C–700 °C R_P activation energies of 0.54 eV and 0.41 eV, respectively. These 650 °C–700 °C "activation energies" should not be taken to represent the energy barrier for a physical process because, as shown by the EIS Nyquist plots of Fig. 3 and the equivalent circuit modeling results of Tables S1 and S2, they result from a nearly temperature-invariant gas concentration polarization resistance becoming a greater percentage of the total electrode response with increased temperature. The lower apparent 650 °C–700 °C E_A for the GDC pre-infiltrated LSCF-GDC, compared to bare LSCF-GDC, resulted from the lower resistance of the high and intermediate frequency EIS arcs (as shown later in Fig. 5), which let the concentration polarization arc (with its temperature invariance) dominate more of the overall response.

Thanks to their nearly identical R_P values over the entire 400 °C–700 °C temperature range, the bare and GDC pre-infiltrated 12 vol% SSC-GDC NCCs produced here both achieved a polarization resistance of 0.1 Ωcm^2 at ∼610 °C, displayed similar 400 °C–650 °C SSC-GDC R_P activation energies of 0.96 and 0.93 eV, respectively, and displayed similar 650 °C–700 °C SSC-GDC R_P activation energies of 0.57 and 0.55 eV, respectively. These 400 °C–650 °C activation energies agreed well with the ∼0.9 eV 400 °C–700 °C E_A reported for SSC-GDC NCCs in the literature,[32] and the 0.8–1.2 eV 400 °C–650 °C E_A reported previously for SSC-$Sm_{0.2}Ce_{0.8}O_{1.9}$ composite cathodes produced with various SSC loading levels and firing conditions.[30] However, they are much less than the 1.3 eV 400 °C–650 °C E_A reported for oxygen surface exchange into dense SSC thin films[6] and the 1.3–1.5 eV E_A reported at or near these temperatures for dense SSC bulk pellets,[39] electrospun SSC,[40] and micro-porous SSC cathodes.[41] This can be explained by considering the low ∼0.6–0.9 eV 400 °C–650 °C E_A for oxygen diffusion through a GDC backbone[10,32,42,43] and previous SIMPLE modeling which showed that ∼12 vol% SSC-GDC NCCs transition between ∼550 °C and ∼650 °C from a low temperature regime where oxygen surface exchange into the SSC is more resistive than oxygen transport through the GDC backbone, to a higher temperature regime where the situation is reversed.[32,34] As with the LSCF-GDC NCCs, based on the EIS spectra of Fig. 3, the 650 °C–700 °C SSC-GDC E_A values were assumed to be apparent values caused by a temperature invariant gas concentration polarization resistance, that was larger for the GDC pre-infiltrated cells (as shown later in Fig. 5), becoming a greater percentage of the total electrode response with increased temperature.

Figure 5 and the corresponding equivalent circuit fits of Table S2 of the Supplemental Materials show that GDC pre-infiltration improved the LSCF-GDC cathodes by reducing both the high frequency infiltrate-backbone interfacial resistance and the intermediate frequency electrode resistance, the latter of which was dominated by oxygen surface exchange into the LSCF below ∼650 °C (as explained in the Fig. 4 discussion). In contrast, Fig. 5 and Table S3 also show that GDC pre-infiltration had only a minor effect on the SSC-GDC EIS Nyquist plot shapes.

Pre- and post-aging comparisons.—Figure 6 shows that in addition to improving the initial performance shown in Fig. 4, GDC pre-infiltration reduced the amount of non-linear 500 h, 650 °C open-circuit LSCF-GDC R_P degradation from ∼37% to ∼6%. In contrast, GDC pre-infiltration had no effect on the initial SSC-GDC R_P or the ∼19% in non-linear R_P degradation observed during 500 h of 650 °C open-circuit aging. Similar to previous reports,[35] relatively small 500-hour R_0 degradation rates of 2% ± 1% were observed for all LSCF-GDC and SSC-GDC NCCs. The cause of these R_0 losses were not investigated here, but they may be caused by impurity accumulation at grain boundaries within the electrolyte, the current collectors, and/or the contact pastes.

Table I indicates that GDC pre-infiltration significantly reduced the amount of surface segregated Sr in both aged and as-produced LSCF-GDC NCCs, but did not have a significant effect on these

Table I. XPS-determined Strontium Concentrations.

	LSCF-GDC [Total Sr]/[La+Sr+Co+Fe]	SSC-GDC [Total Sr]/[Sm+Sr+Co]	LSCF-GDC [Surface Sr]/[Total Sr]	SSC-GDC [Surface Sr]/[Total Sr]	LSCF-GDC [Surface Sr]/[La+Sr+Co+Fe]	SSC-GDC [Surface Sr]/[Sm+Sr+Co]
Before 650 °C Aging, Without GDC Pre-Infiltration	0.46 ± 0.05	0.63 ± 0.05	63% ± 10%	60% ± 10%	0.29 ± 0.08	0.38 ± 0.10
Before 650 °C Aging, With GDC Pre-Infiltration	0.16 ± 0.05	0.58 ± 0.05	38% ± 10%	57% ± 10%	0.06 ± 0.04	0.33 ± 0.10
After 650 °C Aging, Without GDC Pre-Infiltration	0.45 ± 0.05	0.63 ± 0.05	51% ± 10%	67% ± 10%	0.23 ± 0.08	0.42 ± 0.10
After 650 °C Aging, With GDC Pre-Infiltration	0.13 ± 0.05	0.64 ± 0.05	62% ± 10%	67% ± 10%	0.08 ± 0.05	0.43 ± 0.10

Note, the "Total Sr" concentration denotes the sum of the "Lattice Sr" concentration and the "Surface Sr" concentration. The error bars in these calculations come from the standard deviations in the concentrations determined from at least three XPS scans on identical samples. The detailed XPS scans and their analyses used to calculate the [Total Sr]/[La+Sr+Co+Fe] ratios can be found in Figs. S2, S3, and Table S4 of the Supplemental Materials. The [Surface Sr]/[Total Sr] percentages were obtained from Sr peak deconvolutions such as that shown in Fig. 7, as described in the Experimental Methods. The [Surface Sr]/[La+Sr+Co+Fe] ratios were calculated by multiplying the two previous quantities.

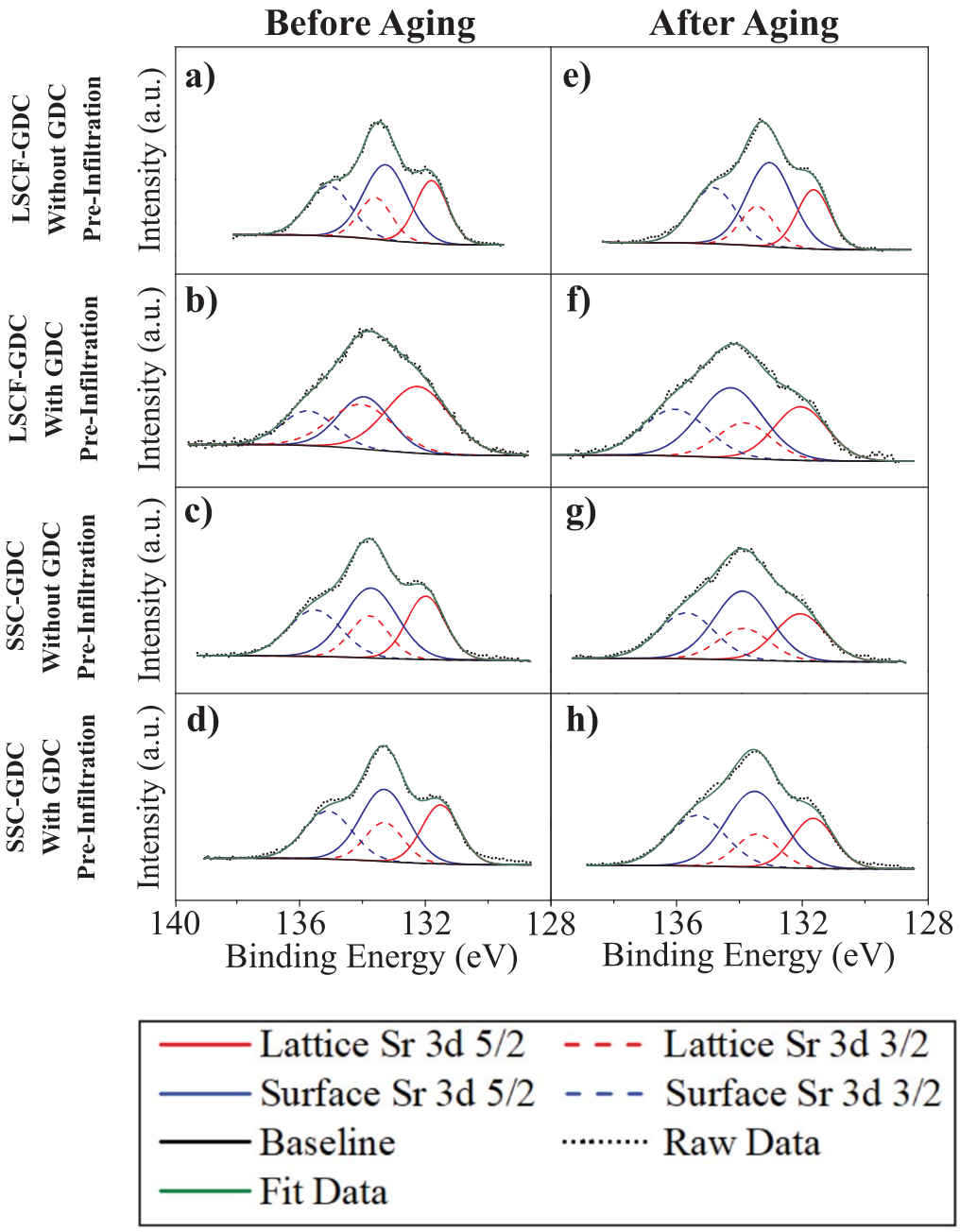

Figure 7. X-Ray Photoelectron Spectroscopy Strontium 3d peak deconvolutions for 12 vol% LSCF-GDC and SSC-GDC NCCs with and without 7.5 vol% of GDC pre-infiltration (a)–(d) before and (e)–(h) after 500 h of 650 °C aging.

concentrations in aged or as-produced SSC-GDC NCCs. Specifically, based on detailed XPS scans such as those shown in Fig. 7, Table I shows that the amount of "Surface" Sr (i.e. Sr which, unlike Sr within the perovskite lattice of LSCF or SSC, is not coordinated with 12 oxygen ions and therefore is either at the crystallographic termination (i.e. the true surface) of the infiltrate, or is in surface precipitates like SrO, $SrCO_3$, etc.) for a given amount of infiltrate (i.e. the [Surface Sr]/[La+Sr+Co+Fe] or the [Surface Sr]/[Sm+Sr+Co] ratio) remained roughly constant during 650 °C aging at ∼0.26 for bare LSCF-GDC and ∼0.40 for bare SSC-GDC. Further, the GDC pre-infiltrated SSC-GDC had roughly the same [Surface Sr]/[Sm+Sr+Co] ratios as the bare SSC-GDC. In contrast, GDC pre-infiltration into LSCF-GDC lowered the [Surface Sr]/[La+Sr+Co+Fe] ratio by nearly a factor of four. This, combined with the Figs. 3–5 discussion that aging increased the LSCF-backbone and LSCF-gas interfacial resistance, suggests that GDC pre-infiltration altered the performance and aging of LSCF-GDC cathodes by scavenging exsolved Sr-rich phases such as SrO from the LSCF-gas and LSCF-backbone interface, but was unable to do so for the SSC-GDC cathodes because SSC does not precipitate out SrO. This interpretation is consistent with the many studies which have observed that Sr surface segregation results in increased Lattice Sr, Surface Sr, and exsolved Sr-rich secondary phases in LSCF,[35,37,44,45] and recent dissolution and ICPMS studies suggesting that SSC does not precipitate out SrO as it degrades over 400 h at 750 °C.[45] However, it is at odds with other studies[30] claiming that ceria additions reduce the interfacial resistance of SSC.

Figure 8 and the corresponding equivalent circuit resistance values reported in Table S3 of the Supplemental Materials show that, similar to its impact on the initial performance of LSCF-GDC and SSC-GDC cathodes, GDC infiltration reduced the severity of the high and intermediate frequency resistance increases observed with

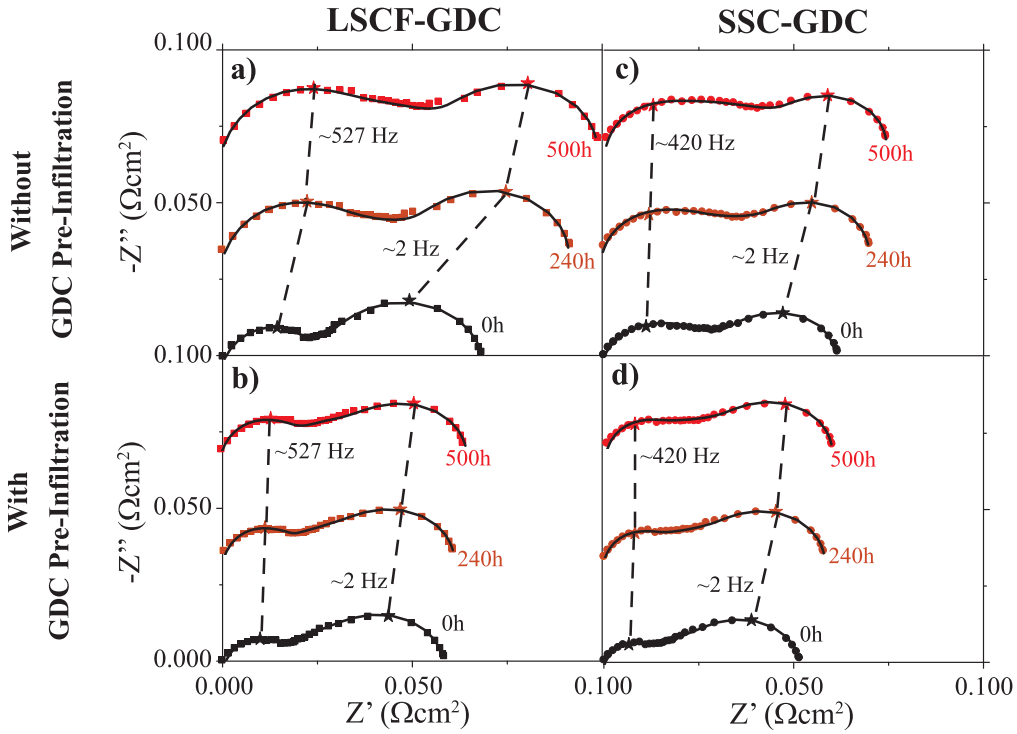

Figure 8. Open Circuit 650 °C Electrochemical Impedance Spectroscopy Nyquist plots for 12 vol% (a)–(b) LSCF-GDC, and (c)–(d) SSC-GDC NCCs with and without GDC pre-infiltration measured in air after various amounts of 650 °C open-circuit aging in air. To ease in comparison, the *x*-axis ohmic offset (which differed by less than 2% between cells) has been removed from the plots. To help the reader identify which frequency regimes are changing with temperature, dashed lines joining points taken at identical frequencies have been added to the plots. High, intermediate and low frequency equivalent circuit resistance values resulting in the fits shown here as black lines are reported in Table S3 of the Supplemental Materials.

aging in LSCF-GDC cathodes, but had less impact on the SSC-GDC electrochemical performance with aging. In addition, GDC pre-infiltration did little to alter the size of the ~2 Hz gas concentration EIS arc in either the LSCF-GDC or SSC-GDC cells.

Figure 9 (and the detailed particle size analyses shown in Figs. S6–S9 and Tables S5–S8 of the Supplemental Materials) indicate that both LSCF-GDC and SSC-GDC NCCs, before and after aging, with and without GDC pre-infiltration contained average infiltrate particle sizes of ~ 40 nm. Even though past studies have suggested that 1) GDC particle size coarsening is responsible for LSCF-GDC[46] and SSC-GDC[36] electrochemical performance degradation with aging, and 2) that GDC pre-infiltration led to LSCF infiltrate particle size reductions,[15] no evidence for either effect was found here. Further, SIMPLE model[12,32,34] predictions indicate that, in order to account for all the R_P degradation shown in Fig. 6, the infiltrate diameters in the various cathodes would have had to increase from 40 nm to 74 nm for bare LSCF-GDC, 40 nm to 45 nm for GDC pre-infiltrated LSCF-GDC, 40 nm to 58 nm for bare SSC-GDC, and 40 to 56 nm for GDC pre-infiltrated SSC-GDC. Since all of these infiltrate particle size changes, except for the GDC pre-infiltrated LSCF-GDC, are large enough to be easily detected via SEM, additional mechanisms, beyond just infiltrate coarsening, must have also been active in the bare LSCF-GDC, SSC-GDC, and GDC pre-infiltrated SSC-GDC.

Discussion

Mechanisms.—Figure 10 summarizes the mechanisms proposed here to explain why GDC pre-infiltration improved the performance of LSCF-GDC, but not SSC-GDC, NCCs. Specifically, as shown in Fig. 10a, the results here suggest that the pre-infiltrated GDC particles scavenged exsolved, surface-segregated Sr-rich phases from the LSCF-GDC and LSCF-gas interfaces. This is consistent with the fact that 1) Sr^{2+} is only a slightly oversized ion with a moderately high 1450 °C solubility limit of ~8 mol% in ceria,[47–50] and 2) the fact that high surface area grain boundaries/interfaces are known to be able to accommodate a large amount of impurity atoms.[51] Further, the XPS and EIS results here, combined with literature results showing that several hundred hours of aging at ~750 °C and below produces both in-lattice surface Sr segregation and SrO secondary phase precipitation in LSCF,[45] but no SrO secondary phase precipitation in SSC,[36] supports the idea that GDC improves the performance of LSCF by scavenging exsolved, surface-segregated Sr-rich phases that are not present in SSC.

Although the results here are consistent with GDC pre-infiltrate scavenging exsolved Sr-rich phases, they are less consistent with some of the alternative GDC-LSCF oxygen exchange rate enhancement theories proposed in the literature. For instance, the fact that the refractory GDC particles are infiltrated and fired before, not after, the LSCF infiltrate (and the fact that the bare LSCF-GDC also contains a high amount of GDC surface area (roughly half as much as GDC pre-infiltrated LSCF-GDC)) makes it unlikely that GDC pre-infiltration improved the LSCF oxygen exchange rate kinetics through surface doping or interface core charge changes (since GDC was not on top of the LSCF). In addition, the fact that the oxygen surface exchange coefficient activation energy for pure GDC below ~650 °C is ~0.6 eV[22] but the GDC pre-infiltrated LSCF-GDC cells exhibited 400 °C–600 °C activation energies of ~1 eV, suggests that the GDC nanoparticles never became active towards oxygen exchange across their surface. This is consistent with the idea that neither the GDC surface impurity cleanup,[24,25] GDC transition metal surface doping,[24] or GDC reaction spillover[17,25,26] mechanisms proposed in the literature occurred here because 1) it is presently unclear why SSC wouldn't also be able to adsorb GDC surface impurities, donate transition metals to the GDC, and/or engage in catalytic spillover, like LSCF, 2) the 400 °C–650 °C R_P activation energies shown in Fig. 4a were unchanged with GDC pre-infiltration, and 3) because it seems unlikely (given the extensive body of literature showing how potent surface Sr segregation is in degrading LSCF oxygen exchange)[52–54] that the impacts on oxygen surface

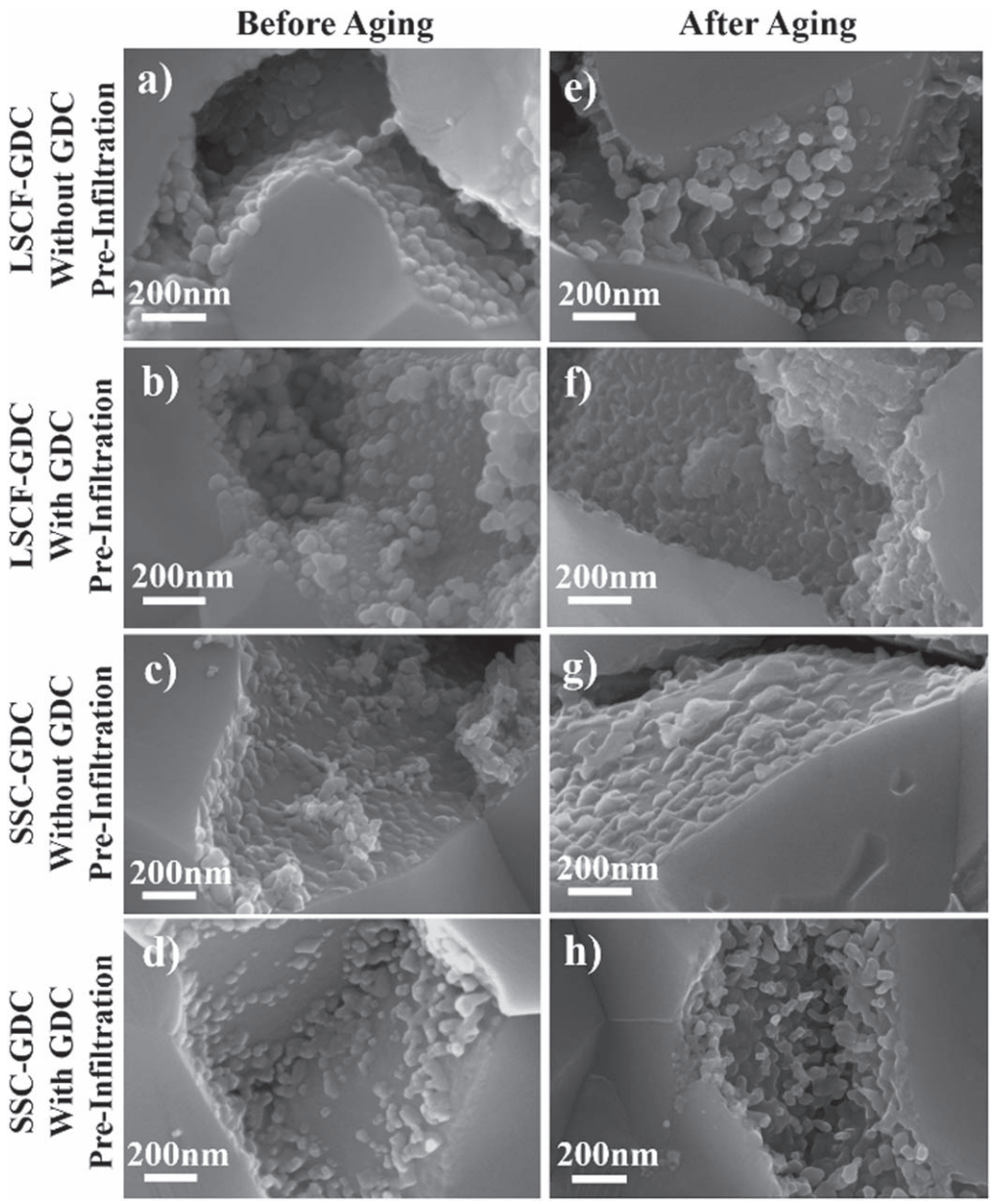

Figure 9. Scanning Electron Microscopy images of 12 vol% LSCF-GDC and SSC-GDC NCCs with and without 7.5 vol% of GDC pre-infiltration (a)–(d) before and (e)–(h) after 500 h of 650 °C aging.

exchange caused by the observed changes in the Sr surface concentration would be overwhelmed by other factors.

Practical implications.—This work has several important practical implications. First, the ability of nano-sized GDC to improve LSCF-GDC NCC performance by scavenging interfacial strontium is similar to the mechanism by which atomic layer deposited (ALD) ZrO_2 overcoats have recently been concluded to improve LSCF-GDC performance.[35] However, GDC pre-infiltration is considerably cheaper and easier to conduct than ALD, especially on large area SOFCs and SOECs. Hence, for those composite electrodes where the electrochemical performance improvements result mainly from the chemical cleaning of various material interfaces, infiltration is likely to be the preferred manufacturing method. Second, even though bare SSC-GDC is more stable than bare LSCF-GDC in Fig. 6 (because it is less prone to form exsolved, surface-segregated, Sr-rich secondary phases), the degradation rates of GDC pre-infiltrated LSCF-GDC NCCs are actually lower than any of the SSC-GDC NCCs. Hence, as long as surface strontium segregation mitigation strategies (such as the GDC pre-infiltration used here) remain active, LSCF-GDC cathodes may actually be the better choice for SOFC/SOEC operation. Lastly, it is important to note that even though GDC pre-infiltration had no effect on the SSC-GDC cathodes tested here under open-circuit conditions for 500 h at 650 °C, GDC pre-infiltration may be useful in preventing SSC degradation at higher temperatures, alternative voltages, and/or longer times if/when SSC begins to precipitate out Sr-rich secondary phases.

Conclusions

Here, EIS and XPS results showed that GDC pre-infiltration improved the 650 °C R_P performance and stability of LSCF-GDC NCCs by enhancing oxygen exchange at the infiltrate-GDC and infiltrate-pore interface through the scavenging of exsolved, surface-segregated, Sr-rich, secondary phases. In contrast, GDC pre-infiltration had no effect on the 650 °C R_P performance or stability of SSC-GDC NCCs. These results, combined with 1) Scanning Electron Microscopy (SEM) results which showed no significant infiltrate

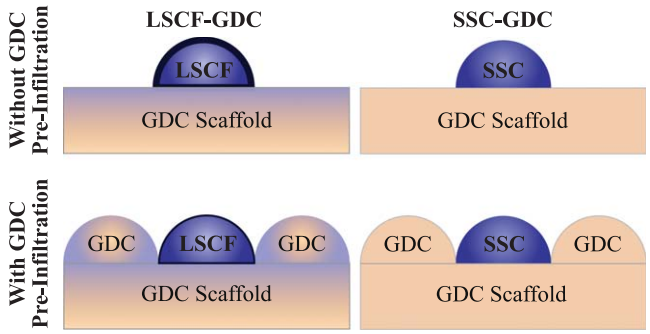

Figure 10. Schematic of the proposed mechanism by which GDC Pre-Infiltration acts. As denoted by the blue shading within the LSCF and SSC, Sr segregates to the exterior fringes of the lattice in both materials during manufacturing, but LSCF also exsolves secondary Sr-rich phases (denoted by the thick outer blue line) that either remain on the surface or disappear when their constituent Sr diffuses into neighboring pre-infiltrated GDC particles. Note, as indicated by the data in Table I, the changes in Sr distribution that occur during 650 °C aging are smaller than the error in the XPS measurements, but are large enough to affect the electrical properties shown in Figs. 3–6. Hence, this figure could represent either the aged or as-produced samples.

particle size differences between LSCF-GDC or SSC-GDC, either with or without GDC pre-infiltration, before or after aging, 2) X-ray Diffraction (XRD) results which showed that GDC pre-infiltration did not significantly alter the phase purity of LSCF or SSC, and 3) recent literature reports[36] that, unlike LSCF,[45] SSC does not precipitate out SrO onto its surface over several hundred hours at or below 750 °C, suggest that GDC pre-infiltration improved the performance and durability of LSCF-GDC by scavenging exsolved Sr-rich secondary phases that form on the surface of LSCF, but not SSC.

Acknowledgments

The LSCF-GDC portion of this work was supported by the Department of Energy Office of Fossil Energy under Award DE-FE0031250. The SSC-GDC portion of this work was supported by Nissan Technical Center North America. Profilometry was conducted at the Michigan State University Keck Microfabrication Facility. SEM and XPS were conducted at the Michigan State University Composite Materials and Structures Center, which is supported by the NSF Major Research Instrumentation Program and Michigan State University.

ORCID

Jason D. Nicholas https://orcid.org/0000-0001-7986-209X

References

1. Z. Shao and S. M. Haile, *Nature*, **431**, 170 (2004).
2. F. Tietz, D. Sebold, A. Brisse, and J. Schefold, *J. Power Sources*, **223**, 129 (2013).
3. A. S. Yu, J. M. Vohs, and R. J. Gorte, *Energy Environ. Sci.*, **7**, 944 (2014).
4. C. O. Park and S. A. Akbar, *J. Mater. Sci.*, **38**, 4611 (2003).
5. J. Sunarso, S. Baumann, J. M. Serra, W. A. Meulenberg, S. Liu, Y. S. Lin, and J. C. D. da Costa, *J. Membr. Sci.*, **320**, 13 (2008).
6. F. S. Baumann, J. Fleig, G. Cristiani, B. Stuhlhofer, H. U. Habermeier, and J. Maier, *J. Electrochem. Soc.*, **154**, B931 (2007).
7. F. S. Baumann, J. Fleig, H. U. Habermeier, and J. Maier, *Solid State Ionics*, **177**, 3187 (2006).
8. H. Xiong, B. K. Lai, A. C. Johnson, and S. Ramanathan, *J. Power Sources*, **193**, 589 (2009).
9. B. T. Dalslet, M. Søgaard, and P. V. Hendriksen, *Solid State Ionics*, **180**, 1050 (2009).
10. M. Mogensen, N. M. Sammes, and G. A. Thompsett, *Solid State Ionics*, **129**, 63 (2000).
11. Z. Gao, L. V. Mogni, E. C. Miller, J. G. Railsback, and S. A. Barnett, *Energy Environ. Sci.*, **9**, 1602 (2016).
12. M. Shah, J. D. Nicholas, and S. A. Barnett, *Electrochem. Commun.*, **11**, 2 (2009).
13. S. P. Jiang, *Mater. Sci. Eng., A*, **418**, 199 (2006).
14. T. E. Burye and J. D. Nicholas, *J. Power Sources*, **276**, 54 (2015).
15. T. E. Burye and J. D. Nicholas, *J. Power Sources*, **300**, 402 (2015).
16. T. E. Burye, H. Tang, and J. D. Nicholas, *J. Electrochem. Soc.*, **163**, F1017 (2016).
17. S. Saher, S. Naqash, B. A. Boukamp, B. Hu, C. Xia, and H. J. M. Bouwmeester, *J. Mater. Chem. A*, **5**, 4991 (2017).
18. L. Zhang, Y. Liu, Y. Zhang, G. Xiao, F. Chen, and C. Xia, *Electrochem. Commun.*, **13**, 711 (2011).
19. M. R. Afshar, N. Yan, B. Zahiri, D. Mitlin, K. T. Chuang, and J. L. Luo, *J. Power Sources*, **274**, 211 (2015).
20. X. Y. Xu, Z. Y. Jiang, X. Fan, and C. R. Xia, *Solid State Ionics*, **177**, 2113 (2006).
21. R. A. Budiman, T. Miyazaki, S. Hashimoto, K. Yashiro, and T. Kawada, *Solid State Ionics*, **286**, 19 (2016).
22. P. S. Manning, J. D. Sirman, and J. A. Kilner, *Solid State Ionics*, **93**, 125 (1997).
23. H. J. M. Bouwmeester, M. W. DenOtter, and B. A. Boukamp, *J. Solid State Electrochem.*, **8**, 599 (2004).
24. J. Druce, H. Tellez, T. Ishihara, and J. A. Kilner, *Faraday Discuss.*, **182**, 271 (2015).
25. S. Ovtar, M. Søgaard, K. Norrman, and P. V. Hendriksen, *J. Electrochem. Soc.*, **165**, F220 (2018).
26. T. Hong, L. Zhang, F. Chen, and C. Xia, *J. Power Sources*, **218**, 254 (2012).
27. M. Choi, I. A. M. Ibrahim, K. Kim, J. Y. Koo, S. J. Kim, J.-W. Son, J. W. Han, and W. Lee, *ACS Appl. Mater. Interfaces*, **12**, 21494 (2020).
28. B. Zhu, B. Y. Wang, Y. Wang, R. Raza, W. Y. Tan, J. S. Kim, P. A. van Aken, and P. Lund, *Nano Energy*, **37**, 195 (2017).
29. H. Chen et al., *ACS Appl. Mater. Interfaces*, **10**, 39785 (2018).
30. C. R. Xia, W. Rauch, F. L. Chen, and M. L. Liu, *Solid State Ionics*, **149**, 11 (2002).
31. Z. L. Zhan, D. Han, T. Z. Wu, X. F. Ye, S. R. Wang, T. L. Wen, S. Cho, and S. A. Barnett, *RSC Adv.*, **2**, 4075 (2012).
32. J. D. Nicholas, L. Wang, A. V. Call, and S. A. Barnett, *Phys. Chem. Chem. Phys.*, **14**, 15379 (2012).
33. T. E. Burye and J. D. Nicholas, *J. Power Sources*, **301**, 287 (2016).
34. J. D. Nicholas and S. A. Barnett, *J. Electrochem. Soc.*, **157**, B536 (2010).
35. Y. Zhang, Y. Wen, K. Huang, and J. D. Nicholas, *ACS Appl. Energy Mater.*, **3**, 4057 (2020).
36. Z. Pingying, R. Ran, C. Zhihao, G. Hongxia, S Zongping, and L. Shaomin, *AICHE Jrnl*, **53**, 3116 (2007).
37. H. Wang, K. J. Yakal-Kremski, T. Yeh, G. M. Rupp, A. Limbeck, J. Fleig, and S. A. Barnett, *J. Electrochem. Soc.*, **163**, F581 (2016).
38. C. Nicollet, A. Flura, V. Vibhu, A. Rougier, J.-M. Bassat, and J.-C. Grenier, *Int. J. Hydrogen Energy*, **41**, 15538 (2016).
39. P. Zeng, R. Ran, Z. Chen, H. Gu, Z. Shao, and S. Liu, **53**, 3116 (2007).
40. C. L. Chang, C. S. Hsu, J. B. Huang, P. H. Hsu, and B. H. Hwang, *J. Alloys Compd.*, **620**, 233 (2015).
41. H. Lv, Y.-j. Wu, B. Huang, B.-y. Zhao, and K.-a. Hu, *Solid State Ionics*, **177**, 901 (2006).
42. B. C. H. Steele, *Solid State Ionics*, **129**, 95 (2000).
43. J. W. Fergus, *J. Power Sources*, **162**, 30 (2006).
44. B. Koo, K. Kim, J. K. Kim, H. Kwon, J. W. Han, and W. Jung, *Joule*, **2**, 1476 (2018).
45. H. Q. Wang, K. J. Yakal-Kremski, T. Yeh, G. M. Rupp, A. Limbeck, J. Fleig, and S. A. Barnett, *J. Electrochem. Soc.*, **163**, F581 (2016).
46. M. Shah, P. W. Voorhees, and S. A. Barnett, *Solid State Ionics*, **187**, 64 (2011).
47. R. D. Shannon, *Acta Crystallogr.*, **A32**, 751 (1976).
48. H. Yahiro, T. Ohuchi, K. Eguchi, and H. Arai, *J. Mater. Sci.*, **23**, 1036 (1988).
49. J. Ranlov, F. W. Poulsen, and M. Mogensen, *Solid State Ionics*, **61**, 277 (1993).
50. J. D. Nicholas and L. C. DeJonghe, *Solid State Ionics*, **178**, 1187 (2007).
51. Y. H. Cho, P. S. Cho, G. Auchterlonie, D. K. Kim, J. H. Lee, D. Y. Kim, H. M. Park, and J. Drennan, *Acta Mater.*, **55**, 4807 (2007).
52. D. Oh, D. Gostovic, and E. D. Wachsman, *J. Mater. Res.*, **27**, 1992 (2012).
53. Y. Yu, K. F. Ludwig, J. C. Woicik, S. Gopalan, U. B. Pal, T. C. Kaspar, and S. N. Basu, *ACS Appl. Mater. Interfaces*, **8**, 26704 (2016).
54. S. P. Simner, M. D. Anderson, M. H. Engelhard, and J. W. Stevenson, *Electrochem. Solid-State Lett.*, **9**, A478 (2006).